ACS Energy LETTERS
http://pubs.acs.org/journal/aelccp

$NaAlCl_4$: New Halide Solid Electrolyte for 3 V Stable Cost-Effective All-Solid-State Na-Ion Batteries

Juhyoun Park, Jun Pyo Son, Wonseok Ko, Jae-Seung Kim, Yeji Choi, Hyungsub Kim, Hiram Kwak, Dong-Hwa Seo, Jongsoon Kim, and Yoon Seok Jung*

Cite This: *ACS Energy Lett.* 2022, 7, 3293−3301 Read Online

ACCESS | Metrics & More | Article Recommendations | Supporting Information

ABSTRACT: Although high-voltage-stable halide solid electrolytes (SEs) have emerged, only a few Na^+ halide SEs have been developed thus far. Moreover, the use of expensive elements reduces the suitability of all-solid-state Na-ion batteries (ASNBs). Herein, the new mechanochemically prepared orthorhombic $NaAlCl_4$ is demonstrated to exhibit a 10-fold enhancement in Na^+ conductivity (3.9×10^{-6} S cm^{-1} at 30 °C) compared to annealed samples. The feasibility of $NaAlCl_4$ for ASNBs is also validated for the first time. X-ray Rietveld refinement with bond valence energy landscape calculations reveals 1D-preferable 2D Na^+ conduction pathways. High-voltage stability up to ∼4.0 V (vs Na/Na^+) is confirmed by electrochemical measurements and theoretical calculations. Furthermore, the outstanding electrochemical performance of $NaCrO_2/Na_3Sn$ ASNBs at 30 and 60 °C is demonstrated (e.g., 82.9% capacity retention at the 500th cycle at 60 °C and 1C), shedding light on the potential of the cost-effective and safe energy storage systems.

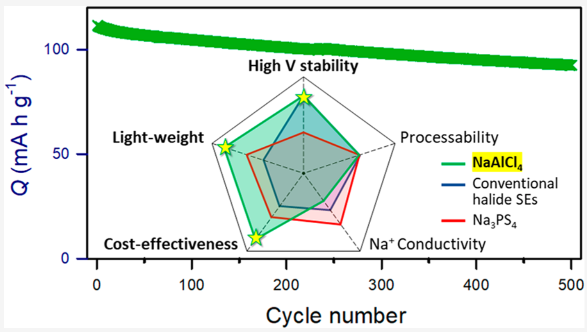

Li-ion batteries (LIBs) have expanded into application areas such as large-scale energy storage systems (ESSs) that could stabilize the power grid.[1,2] However, the price of Li rose more than 10-fold over the past decade (from 6.06 USD kg^{-1} in 2012 to 75 USD kg^{-1} in 2022 for Li_2CO_3).[3] In addition, the uneven distribution of Li mines has caused political and economic issues.[4−7] Moreover, there are safety concerns about LIBs, as seen from frequent fire accidents associated with the use of flammable organic liquid electrolytes.[8−10] These factors have impeded the widespread use of LIBs for ESSs.[8,9,11] Solidifying electrolytes with nonflammable inorganic Na^+ superionic conductors could improve safety and reduce cost, making all-solid-state Na-ion or Na batteries (ASNBs) promising for use as ESSs.[4,12−26]

Sulfide SEs have been extensively investigated due to their high ionic conductivity and mechanical deformability which allows for the cold-pressing-based fabrication of all-solid-state batteries.[12−19,24,27−32] The first sulfide Na^+ superionic conductor, cubic Na_3PS_4, had a Na^+ conductivity of 0.2 mS cm^{-1}.[13] Since then, various aliovalent and/or isovalent substitutions for Na_3PS_4 have been investigated, which produced compounds with improved Na^+ conductivity,[15−19,24,30,33] including Na_3SbS_4 (1 mS cm^{-1}), $Na_{1-2x}Ca_xPS_4$ (1 mS cm^{-1}), $Na_{3-x}PS_{4-x}Cl_x$ (1 mS cm^{-1}), and $Na_{3-x}Sb_{1-x}W_xS_4$ (maximum ∼40 mS cm^{-1}). However, the electrochemical oxidation stability of sulfide SEs is as low as ∼2 V (vs Na/Na^+).[25,28]

Recently, halide SEs have emerged as a game changer because they are mechanically sinterable, similarly to sulfide SEs, and exhibit excellent electrochemical oxidation stability and interfacial compatibility with $LiMO_x$ (M = Ni, Co, Mn, and Al mixture) cathode active materials (CAMs).[31,34,35] Since the seminal report on Li_3YCl_6 (0.5 mS cm^{-1}) that demonstrated stable cycling of $LiCoO_2$ with a high initial Coulombic efficiency (ICE) of 94.8%, several new Li^+ halide SEs have been developed, including Li_3YCl_6,[35] Li_3InCl_6,[36] Li_xScCl_{3+x},[37,38] Li_2ZrCl_6,[39,40] $Li_{3-x}M_{1-x}Zr_xCl_6$ (M = Y, Er),[41] $Li_{3-x}Yb_{1-x}M_xCl_6$ (M = Zr, Hf),[42,43] etc.[44−46] However, only three Na^+ analogues have been identified experimentally thus far: Na_2ZrCl_6,[25] $Na_{3-x}Er_{1-x}Zr_xCl_6$,[23] and $Na_{3-x}Y_{1-x}Zr_xCl_6$.[47] A

Received: July 2, 2022
Accepted: August 31, 2022
Published: September 7, 2022

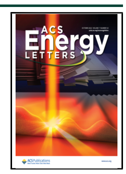

https://doi.org/10.1021/acsenergylett.2c01514
ACS Energy Lett. 2022, 7, 3293−3301

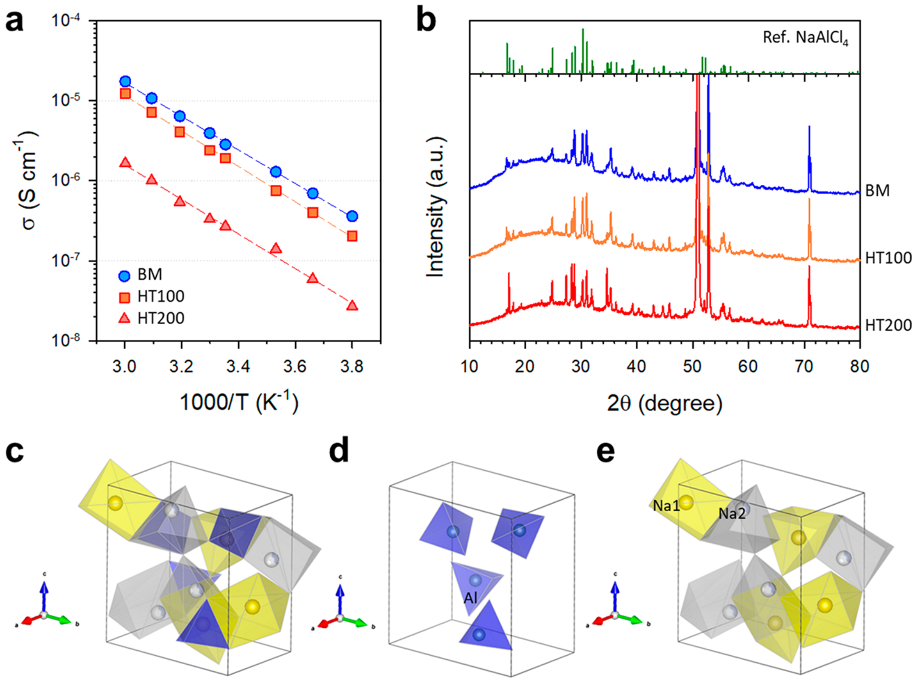

Figure 1. Characterization of BM-, HT100-, and HT200-$NaAlCl_4$. (a) Arrhenius plots of Na^+ conductivity and (b) powder XRD patterns. (c) Crystal structure of BM-$NaAlCl_4$ with the unit cell outlined. Corresponding crystal structures built up by (d) $AlCl_4^-$ and (e) $NaCl_6^{5-}$.

criticism for the practical applications of halide SEs is the use of rare and expensive central metals such as Y, In, and Sc.[34] This is even more critical for Na^+ halide SEs because the use of costly elements severely offsets the cost-effectiveness of Na chemistry. This motivated us to explore compositions using cheap and earth-abundant elements, such as Al (Figure S1).

A $NaCl-AlCl_3$ binary system has long been the key for diverse research fields, including rechargeable Na batteries.[48,49] $NaAlCl_4$ melts at ~160 °C and can consequently be used as a molten salt electrolyte for high-temperature-operating Na−$NiCl_2$[2,22,50,51] and Na−Al[52−55] batteries for ESSs. In addition, $NaAlCl_4-nSO_2$ is a nonflammable inorganic liquid electrolyte at room temperature (RT).[56,57] As such, the properties of $NaAlCl_4$ and the corresponding battery performance have been investigated in the molten state at elevated temperatures or in an inorganic liquid state ($NaAlCl_4-nSO_2$), thus far without any reports on solid-state Na^+ conduction for ASNBs.

In this study, we demonstrate the suitability of $NaAlCl_4$ for ASNBs operating at RT. Mechanochemically prepared orthorhombic $NaAlCl_4$ (space group of $P2_12_12_1$) exhibited an Na^+ conductivity of 3.9×10^{-6} S cm^{-1} at 30 °C, which was 1 order of magnitude higher than that of its highly crystalline counterpart obtained by annealing at elevated temperatures. X-ray Rietveld refinement and bond valence energy landscape (BVEL) analyses revealed two prismatic Na^+ sites, among which one-dimensional (1D)-preferable 2D Na^+ migration pathways were formed. First-principles calculations, cyclic voltammetry (CV), and stepwise high-voltage tests showed the high oxidation stability limit of $NaAlCl_4$ at a minimum of ~4.0 V (vs Na/Na^+). $NaCrO_2/Na_3Sn$ ASNBs employing BM-$NaAlCl_4$ demonstrated excellent cycling performance at 30 and 60 °C despite relatively low Na^+ conductivity. Cycling performances of 82.0% and 82.9% capacity retention were achieved at 30 °C (0.2C, 300 cycles) and 60 °C (1C, 500 cycles), respectively.

Three $NaAlCl_4$ samples were prepared by mechanochemical milling of an equimolar $NaCl-AlCl_3$ mixture without or with subsequent heat treatment (HT) at 100 or 200 °C, and are referred to as BM-, HT100-, and HT200-$NaAlCl_4$, respectively. The Na^+ conductivities of the resulting cold-pressed pellets were measured by the AC impedance method using Na^+-blocking Ti/SE/Ti symmetrical cells. Arrhenius plots of Na^+ conductivity are shown in Figure 1a. Nyquist plots of BM-$NaAlCl_4$ are shown in Figure S2. BM-$NaAlCl_4$ exhibited a Na^+ conductivity of 3.9×10^{-6} S cm^{-1} at 30 °C with an activation energy of 0.42 eV. The electronic conductivity of BM-$NaAlCl_4$, measured by chronoamperometry, was 1.2×10^{-10} S cm^{-1} (Figure S3), which translates into a transference number of close to unity. Moreover, this value is much lower than that of sulfide SEs (~10^{-9} S cm^{-1}), which is highly advantageous for suppressing side reactions.[58,59] The excellent deformability of BM-$NaAlCl_4$ was also confirmed by the flattened surface of cold-pressed pellets prepared under 370 MPa (Figure S4). As the annealing temperature for BM-$NaAlCl_4$ was increased to 100 and 200 °C, the Na^+ conductivity gradually decreased to 2.4×10^{-6} and 3.3×10^{-7} S cm^{-1}, respectively. The latter is 10-fold lower compared to that without annealing.[60] The significant enhancement in Na^+ conductivity for BM-$NaAlCl_4$ compared to annealed samples is comparable to that of various halide SEs, such as $LiAlCl_4$,[61] Li_3YCl_6,[35] and Li_2ZrCl_6,[39] which is explained by ionic conduction channels and energy landscapes rendered by cationic disorders[44,62,63] and/or stacking faults.[46]

The powder X-ray diffraction (XRD) patterns of all three samples shown in Figure 1b matched the Bragg peaks of orthorhombic $NaAlCl_4$ with a space group of $P2_12_12_1$.[64] Although the XRD crystallinities for BM- and HT100-$NaAlCl_4$ were similar, HT200-$NaAlCl_4$ presented a notable increase in XRD crystallinity. Considering the low melting temperature of ~160 °C for $NaAlCl_4$, the high crystallinity of HT200-$NaAlCl_4$ originates from the recrystallization of $NaAlCl_4$ melts. The

https://doi.org/10.1021/acsenergylett.2c01514
ACS Energy Lett. 2022, 7, 3293−3301

BM- and HT100-$NaAlCl_4$ samples were powdery, whereas the HT200-$NaAlCl_4$ sample existed as a solid mass (Figure S5). The low melting point of 152 °C for $NaAlCl_4$ was confirmed by a differential scanning calorimetry result (Figure S6).

The powder XRD Rietveld refinement profiles of BM-$NaAlCl_4$ and HT200-$NaAlCl_4$ are shown in Figure S7, and the corresponding results are summarized in Tables S1 and S2. The fitted results of BM-$NaAlCl_4$ showed a density of 2.02 g cm^{-3} (a = 6.17302 Å, b = 9.88428 Å, c = 10.33293 Å, V = 630.5 $Å^3$). Notably, this value is significantly lower than those of other Na^+ halide SEs (Na_2ZrCl_6, 2.43 g cm^{-3}; $Na_{2.8}Er_{0.8}Zr_{0.2}Cl_6$, 2.84 g cm^{-3}) and is slightly lower than that of the sulfide SE Na_3PS_4 (2.19 g cm^{-3}),[13] indicating an advantage in the specific energy density of ASNBs with $NaAlCl_4$. The crystal structure of $NaAlCl_4$ is shown in Figure 1c−e. Al^{3+} is located at the tetrahedral site to form $AlCl_4^-$ tetrahedra that are isolated from one another (Figure 1d). In Li_3MCl_6 (M = Y, Er, In, Sc, Zr), MCl_6^{3-} octahedra form the structural framework.[34−36,39,44,65] The occurrence of the $AlCl_4^-$ tetrahedra in $NaAlCl_4$ is due to the smaller ionic radius of Al^{3+} (crystal ionic radius of 53 pm) compared to others for Li_3MCl_6 (86−103 pm).[66] Na^+ is positioned in two different prismatic sites denoted as "Na1" and "Na2" sites in BM-$NaAlCl_4$, which were previously reported and newly identified in this study, respectively (Figure 1e). On the other hand, for HT200-$NaAlCl_4$, the best refinement result at a reliable level (χ = 6.95) was obtained for a model without the Na2 site. When the Na2 site was added, the χ value increased to 7−8, indicating that the structure model without the Na2 site occupation is more appropriate for the highly crystalline HT200-$NaAlCl_4$. The dispersed Na^+ occupation in BM-$NaAlCl_4$ is similar to that in other mechanochemically prepared halide SEs, such as Na_2ZrCl_6, Li_2ZrCl_6, Li_3YCl_6, and Li_3ErCl_6.[25,34,39,44] First-principles calculations revealed that the structure which has all Na^+ in the Na1 site is energetically more favorable than those for which Na^+ is distributed in both Na1 and Na2 sites. However, their energy differences are only 5−53 meV/atom (Tables S3 and S4), supporting Na^+ occupation in the Na2 site for the mechanochemically prepared sample BM-$NaAlCl_4$. A more detailed description is provided later.

Further structural information was acquired by Raman spectroscopy (Figure S8). The precursor $AlCl_3$ showed a peak at 310 cm^{-1}, corresponding to three-way intersectional $AlCl_6^{3-}$ octahedra sharing three edges with their neighbors (Figure S9).[65] BM- and HT-$NaAlCl_4$ exhibited peaks at 350 cm^{-1} without any signals of $AlCl_3$. The characteristic peaks at 350 cm^{-1} correspond to the vibration of the $AlCl_4^-$ tetrahedra (A_1 mode).[23,67,68,69] ^{23}Na magic angle spinning nuclear magnetic resonance (MAS NMR) spectra for BM-$NaAlCl_4$ at various temperatures are shown in Figure S10.

A BVEL analysis was performed to assess the Na^+ migration pathways in BM-$NaAlCl_4$ (Figure 2). Despite its inaccuracy, soft BV provides a suitable approximation of the relative height of the barriers and ion migration pathways.[70] Three different Na^+ migration mechanisms between the Na1 and Na2 sites were identified: (i) through a shared rectangular face between face-sharing prisms (transition I, Figure 2a), (ii) through rectangular faces between corner-sharing prisms (transition II, Figure 2b), and (iii) through a triangular face of the Na1 site and a rectangular face of the Na2 site between the corner-sharing prisms (transition III, Figure 2c). The BV isosurface mapping and BVEL calculation results indicate that the

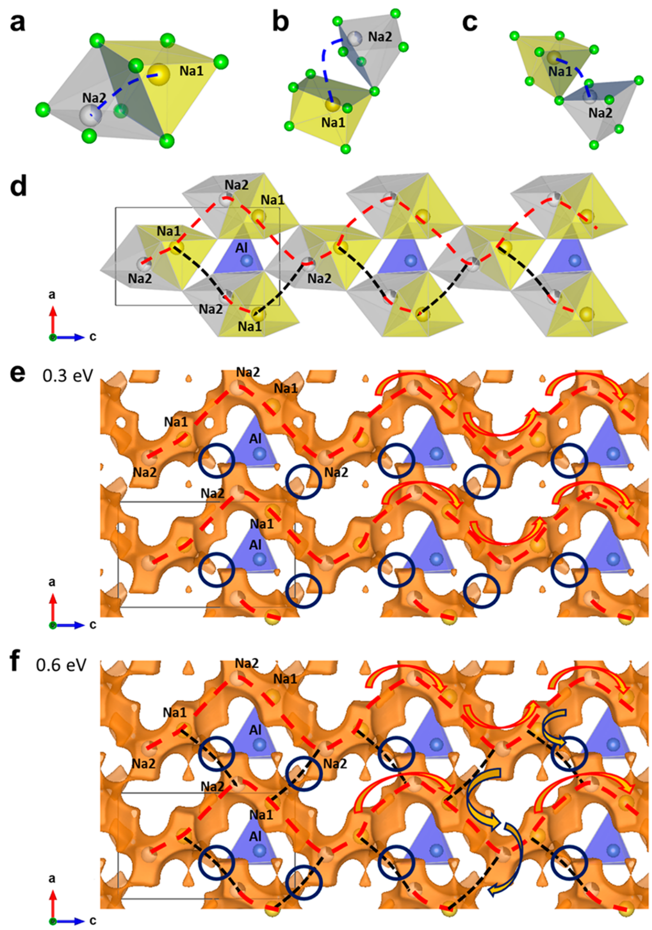

Figure 2. BVEL calculation results of BM-$NaAlCl_4$. (a−c) Three different Na^+ migration mechanisms (transitions I−III) showing colored pathways and a transitional area. (d) Na^+ diffusion pathways viewed in the [010] direction confirmed by the bond valence isosurface mapping. Isosurface maps (e) for 0.3 eV with a 1D diffusion Na^+ pathway and (f) for 0.6 eV with a 2D Na^+ diffusion pathway.

transition modes are more favorable in the descending order transition I > transition II ≫ transition III, which could be understood by considering the much smaller transitional triangular area (6.7 $Å^2$) for transition III than the rectangular transitional area (14.7 $Å^2$). These three types of transition mechanisms were combined to form 2D Na^+ migration pathways in the ac plane (Figure 2d). Figure 2e,f displays the bond valence isosurface maps viewed in the [010] direction with isosurface values of 0.3 and 0.6 eV, respectively. For the map with 0.3 eV, a zigzag-shaped 1D pathway along the [001] direction is formed via transitions I and II (red dashed lines, Figure 2e). For the map with 0.6 eV, the aforementioned 1D pathways are interconnected by transitions I−III (dark blue dashed lines), forming an extended 2D network pathway (Figure 2f). In sharp contrast, a BV isosurface map in the ab plane displays disconnection along the [010] direction (Figure S11), confirming the 1D-preferable 2D Na^+ migration pathways of BM-$NaAlCl_4$. The Na2 site was newly identified in the mechanochemically prepared $NaAlCl_4$, and occupation of the Na2 site would enhance the connectivity of the Na^+ pathways. This could indicate that the occurrence of Na^+ occupation in the Na2 site in the mechanochemically prepared $NaAlCl_4$ may be the key to the remarkably enhanced Na^+

https://doi.org/10.1021/acsenergylett.2c01514
ACS Energy Lett. 2022, 7, 3293−3301

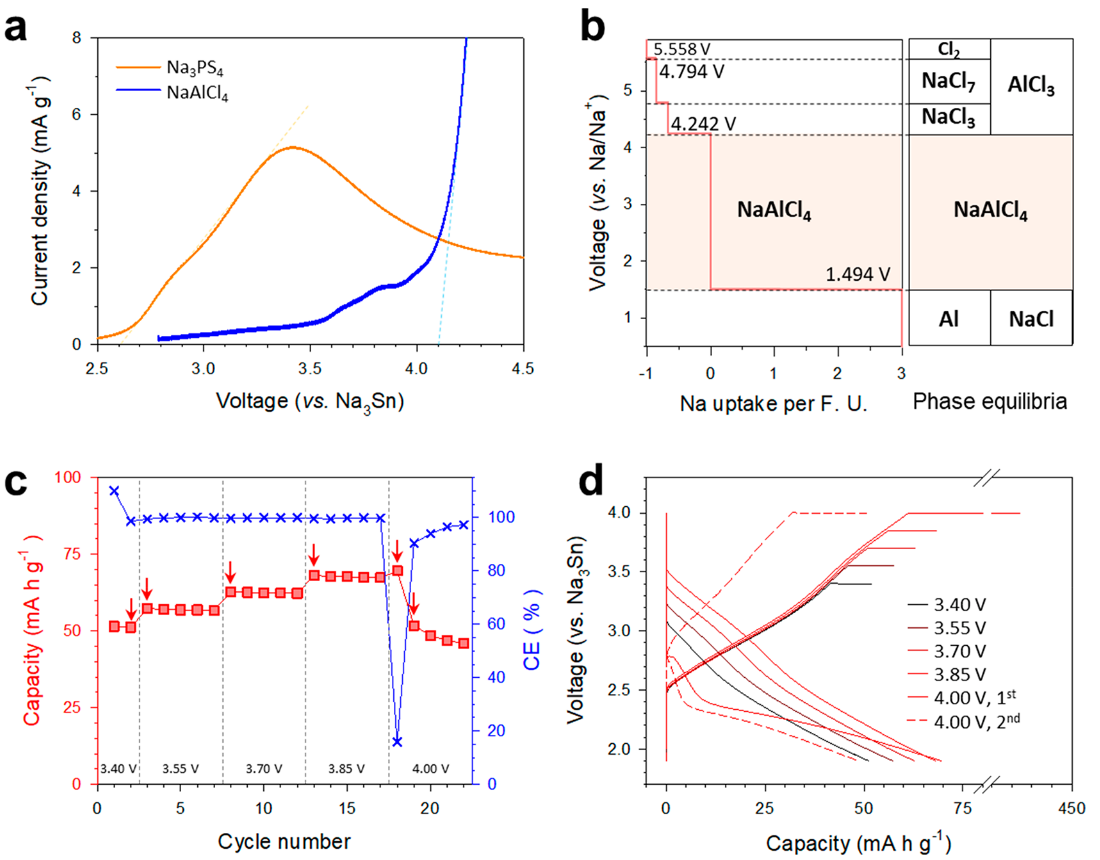

Figure 3. Electrochemical stability of BM-$NaAlCl_4$. (a) Cyclic voltammograms of Na_3PS_4 and BM-$NaAlCl_4$ at 0.1 mV s^{-1} and 30 °C. (b) Phase equilibria of $NaAlCl_4$ as a function of Na/Na$^+$ potential based on first-principles calculations. (c) Discharge capacity and Coulombic efficiency as a function of cycle at 30 °C and 0.1C for $Na_{0.67}Ni_{0.1}Co_{0.1}Mn_{0.8}O_2$ (NaNCM118)/Na_3Sn all-solid-state cells employing BM-$NaAlCl_4$ as the catholyte with a stepwise-increasing upper cutoff voltage from 3.40 to 4.00 V (vs Na_3Sn). (d) Charge−discharge voltage profiles corresponding to those at the cycles indicated by the arrows in (c).

conductivity compared to the highly crystalline annealed sample.[25,40,61]

The electrochemical stability of BM-$NaAlCl_4$ was assessed by cyclic voltammetry (CV) measurements of an SE-C mixture electrode (7:3 wt ratio) at 30 °C. Figure 3a shows the first positive-scan curves of BM-$NaAlCl_4$ and Na_3PS_4. The second and third scan profiles are also shown in Figure S12. The onset potential for severe oxidation of BM-$NaAlCl_4$ was ~4.1 V (vs $Na_3Sn \approx 4.0$ V vs Na/Na$^+$), which is in sharp contrast to ~2.6 V (vs $Na_3Sn \approx 2.5$ V vs Na/Na$^+$) for Na_3PS_4. Moreover, the integrated oxidation current up to 4.0 V (vs Na/Na$^+$) for BM-$NaAlCl_4$ was considerably lower (0.83 mA V g^{-1}) than that for Na_3PS_4 (4.72 mA V g^{-1}), exhibiting the exceptional superiority in oxidation stability of the halide SE $NaAlCl_4$ compared to a sulfide variant. Like other halide SEs,[34,35] BM-$NaAlCl_4$ exhibited a poor reduction stability with the onset reduction current at approximately 2.1 V (vs $Na_3Sn \approx 2.0$ V vs Na/Na$^+$, Figure S12). First-principles calculations were also carried out to reveal the intrinsic electrochemical stability and decomposition products of $NaAlCl_4$. The calculated electrochemical window and phase equilibrium of $NaAlCl_4$ are presented in Figure 3b. $NaAlCl_4$ shows a wide electrochemical window from 1.494 to 4.242 V (vs Na/Na$^+$), and the decomposition products at the anodic limit are predicted to be $NaCl_3$ and $AlCl_3$ phases. Because $NaCl_3$ and $NaCl_7$ are known to be formed at high pressure,[71] the electrochemical stability excluding those phases is also presented in Table S5. The onset voltage of the anodic (oxidation) reaction is consistent with the CV results in Figure 3a. This high oxidative stability verified by both experiments and calculations results manifests $NaAlCl_4$ as a promising SE for high-voltage ASNBs.

To assess the practical electrochemical stability of $NaAlCl_4$ for using $NaMO_2$ CAMs, $Na_{0.67}Ni_{0.1}Co_{0.1}Mn_{0.8}O_2$ (NaNCM118) was selected as a model CAM because of its reversibility up to ~4.5 V (vs Na/Na$^+$) or higher,[72,73] which is consistent with the cell test result of NaNCM118 cathodes using conventional liquid electrolytes (Figure S13). The crystal structure of NaNCM118 is shown in Figure S14 and Table S6. NaNCM118/Na_3Sn all-solid-state cells using BM-$NaAlCl_4$ as the catholyte were cycled with the higher cutoff voltages increasing stepwise by 0.15 V from 3.50 to 4.10 V (vs. Na/Na$^+$), while the lower cutoff voltage was fixed at 2.0 V (vs Na/Na$^+$). The discharge capacity and Coulombic efficiency as a function of the number of cycles are shown in Figure 3c. NaNCM118 with BM-$NaAlCl_4$ retained a stable cycling and a Coulombic efficiency (CE) of close to 100% until the cutoff voltage reached 3.95 V (vs Na/Na$^+$). However, as soon as charging started with a cutoff voltage of 4.10 V (vs Na/Na$^+$) (18th cycle), the charge capacity increased ~6 times (440 vs 70 mA h g^{-1}) and the CE dropped to 15.9% from 99.7%, indicating severe side reactions of $NaAlCl_4$. The corresponding charge−discharge voltage profiles in Figure 3d also show a large overpotential, especially during the first discharge, with a cutoff voltage of 4.10 V (vs Na/Na$^+$). The capacity at the

https://doi.org/10.1021/acsenergylett.2c01514
ACS Energy Lett. 2022, 7, 3293−3301

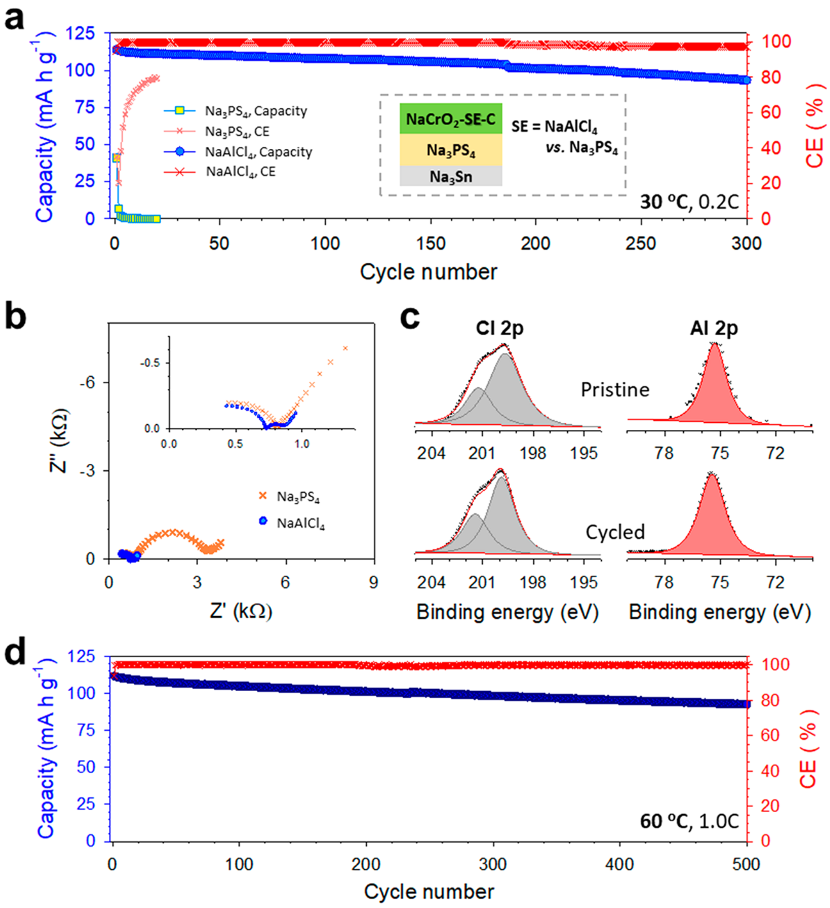

Figure 4. Electrochemical performance of $NaCrO_2/Na_3Sn$ all-solid-state Na-ion batteries (ASNBs) employing a BM-$NaAlCl_4$ catholyte. (a) Cycling performance at 30 °C and 0.2C for $NaCrO_2$ electrodes employing BM-$NaAlCl_4$ or Na_3PS_4. (b) Corresponding Nyquist plots at the first cycle. (c) *Ex situ* XPS signals of $NaCrO_2$ electrodes using BM-$NaAlCl_4$ before and after 20 cycles at 30 °C. (d) Cycling performance for $NaCrO_2$ electrodes employing BM-$NaAlCl_4$ at 60 °C and 1C.

subsequent cycle abruptly decreased. These results indicate that the practical cutoff voltage limit of $NaAlCl_4$ is ~3.95 V (vs Na/Na^+), which agrees well with the CV and first-principles calculations result (Figure 3a,b).

Finally, the feasibility of BM-$NaAlCl_4$ as the catholyte for 3 V class $NaCrO_2/Na_3Sn$ ASNBs was assessed and compared with that of Na_3PS_4 (Figure 4). Na_3PS_4, with a Na^+ conductivity of 1.0×10^{-4} S cm^{-1}, was used as the separating SE layer. Figure 4a shows the cycling performance between 2.0 and 3.5 V at 30 °C and 0.2C in the constant current−constant voltage (CCCV) charging mode (limiting current density of 0.02 C). The corresponding charge−discharge voltage profiles of $NaCrO_2$ with BM-$NaAlCl_4$ are shown in Figure S15. $NaCrO_2$ with Na_3PS_4 showed a low ICE of 35.2% and low discharge capacity of 41 mA h g^{-1}. Its initial capacity decreased substantially in the subsequent cycles. The poorer performance compared to that in previous studies originates from the harsh CCCV charging mode and the presence of conducting carbon additives, where side reactions are accelerated.[25,74,75] In contrast, $NaCrO_2$ electrodes using BM-$NaAlCl_4$ exhibited a high first discharge capacity of 114 mA h g^{-1} and a high ICE of 95.2%, with an excellent capacity retention of as high as 82.0% after 300 cycles. The resistance components in the ASNB cells at different cycles were analyzed by electrochemical impedance spectroscopy (EIS) (Figure 4b and Figure S16). Nyquist plots show an incomplete high-frequency semicircle and a full midfrequency semicircle, which are attributed to the resistances of the separating SE layer and the interfaces of the cathodes, respectively.[25,31,39] The equivalent circuit model and fitted results are provided in Figure S17 and Table S7, respectively. The comparable amplitudes of $R_1 + R_2$ for ASNB cells with BM-$NaAlCl_4$ and Na_3PS_4 (approximately 700−800 Ω) were because they employed the same Na_3PS_4 separating SE layers. In contrast, the interfacial resistances when BM-$NaAlCl_4$ was used were far lower than those when Na_3PS_4 was used (e.g., 116 vs 2405 Ω at the first cycle). Moreover, the amplitude of Na_3PS_4 exceeded that of the SE layer and increased substantially upon cycling (to 6334 Ω at the fifth cycle). The result of the much smaller interfacial resistances in using BM-$NaAlCl_4$ compared to using Na_3PS_4 is surprising considering the lower Na^+ conductivity of BM-$NaAlCl_4$ (3.9×10^{-6} S cm^{-1}) compared to Na_3PS_4 (1.0×10^{-4} S cm^{-1}).

The underlying interfacial evolution was probed by X-ray photoelectron spectroscopy (XPS) measurements of the $NaCrO_2$ electrodes employing BM-$NaAlCl_4$ and Na_3PS_4 before and after 20 cycles at 30 °C (Figure 4c and Figure S18). For the electrodes using Na_3PS_4, both S 2p and P 2p XPS spectra revealed the evolution of the oxidized species SO_4^{2-}, PO_4^{3-}, bridging sulfur (P-[S]$_n$-P), and P_2S_5 (Figure S18).[25] In contrast, for the electrodes using BM-$NaAlCl_4$, marginal changes in both Cl 2p and Al 2p spectra were observed after 20 cycles (Figure 4c), verifying that $NaAlCl_4$ remained intact. Thus, the governing factor for the performance of ASNB cells is the electrochemical and interfacial stability rather than the

https://doi.org/10.1021/acsenergylett.2c01514
ACS Energy Lett. 2022, 7, 3293−3301

ionic conductivity. The kinetic overpotential due to the low electronic conductivity of BM-$NaAlCl_4$ (1.2×10^{-10} S cm^{-1}) would also contribute to the excellent stability.[59] However, when the electrode mass loading was doubled from 11.3 to 22.6 mg cm^{-2}, a substantial increase in the overpotential was observed, which calls for the need to enhance the Na^+ conductivity of the catholyte (Figure S19). The voltage profiles, Nyquist plots, and cycling performance of $NaCrO_2$ cathodes using Na_3PS_4 in the CC or CCCV mode are also provided in Figure S20.

The rate capability results for BM-$NaAlCl_4$ at 30 and 60 °C are shown in Figure S21. The discharge capacity at 0.5C was ≤70 mA h g^{-1} at 30 °C, which was attributed to the low Na^+ conductivity of the BM-$NaAlCl_4$ catholyte. By elevating the temperature to 60 °C, where Na^+ conductivity is boosted to 1.7×10^{-5} S cm^{-1}, the discharge capacity increases, reaching ∼100 mA h g^{-1} at 1C. Based on this result, $NaCrO_2/Na_3Sn$ ASNBs employing the BM-$NaAlCl_4$ catholyte were cycled at 60 °C and 1C (Figure 4d and Figure S22). The ICE was 94.0%, and the average CE in the subsequent cycles was as high as 99.93%. The ASNBs also showed an exceptionally high long-term cycling retention of 82.0% after 500 cycles, with an initial discharge capacity of 112 mA h g^{-1}. In comparison with previous results for ASNBs with $NaCrO_2$, our results demonstrate outstanding performance (Table S8).

In summary, the suitability of orthorhombic $NaAlCl_4$ for RT-operated ASNBs was demonstrated for the first time. The mechanochemically prepared $NaAlCl_4$ exhibited a Na^+ conductivity of 3.9×10^{-6} S cm^{-1} at 30 °C, which was more than 1 order of magnitude higher than that of annealed $NaAlCl_4$ with a low electronic conductivity of 1.2×10^{-10} S cm^{-1}. The BVEL calculation results revealed 1D-preferable 2D Na^+ migration in the *ac* plane through the newly found Na^+ interstitial site. The high electrochemical oxidation voltage limit of $NaAlCl_4$ was as much as ∼4 V (vs Na/Na^+) and was revealed complementarily by first-principles calculations, CV, and stepwise-increasing voltage tests using NaNCM118 cathodes. $NaCrO_2/Na_3Sn$ ASNBs with BM-$NaAlCl_4$ showed much better performance compared to those with Na_3PS_4, emphasizing the decisive role of electrochemical and interfacial stability. Finally, the outstanding cycling stability of $NaCrO_2/Na_3Sn$ ASNBs using the BM-$NaAlCl_4$ catholyte was highlighted at 30 and 60 °C: capacity retentions of 82.0% and 82.9% after 300 cycles at 30 °C and after 500 cycles at 60 °C, respectively. Excellent electrochemical performance was demonstrated using cost-effective elements of Al with Na, highlighting the promising prospect for ESS applications. However, the low Na^+ conductivity of BM-$NaAlCl_6$ should be enhanced to improve its rate capability at RT with higher-areal-capacity electrodes. There may be plentiful opportunities for further enhancement of Na^+ conductivity, as are the cases for Na^+ sulfide and Li^+ halide analogues of Na_3PS_4 and Li_3YCl_6, respectively.

■ ASSOCIATED CONTENT

Supporting Information

The Supporting Information is available free of charge at https://pubs.acs.org/doi/10.1021/acsenergylett.2c01514.

Experimental methods, cost and earth abundance for metals, Nyquist plots, chronoamperometry, SEM image of BM-$NaAlCl_4$, photographs of HT100- and HT200-$NaAlCl_4$, DSC results, XRD Rietveld refinement profiles for BM- and HT200-$NaAlCl_4$, crystal structure of $AlCl_3$, Raman and ^{23}Na MAS NMR spectra, BV isosurface map of BM-$NaAlCl_4$, cyclic voltammogram, electrochemical performance of NaNCM118/Na cells with liquid electrolytes, crystal structure and XRD Rietveld refinement profile for NaNCM118, equivalent circuit model for EIS fitting, electrochemical performance of a $NaCrO_2/Na_3Sn$ all-solid-state cell with high mass loading, electrochemical performance of $NaCrO_2/Na_3Sn$ cells with Na_3PS_4, rate performance of a $NaCrO_2/Na_3Sn$ cell with BM-$NaAlCl_4$, XRD Rietveld refinement result, calculated energy differences and atomic positions before structure relaxation, calculated electrochemical stability range of $NaAlCl_4$, fitted EIS result, and electrochemical performance of ASNBs using $NaCrO_2$ (PDF)

■ AUTHOR INFORMATION

Corresponding Author

Yoon Seok Jung − *Department of Chemical and Biomolecular Engineering, Yonsei University, Seoul 03722, South Korea;* orcid.org/0000-0003-0357-9508; Email: yoonsjung@yonsei.ac.kr

Authors

Juhyoun Park − *Department of Chemical and Biomolecular Engineering, Yonsei University, Seoul 03722, South Korea*

Jun Pyo Son − *Department of Chemical and Biomolecular Engineering, Yonsei University, Seoul 03722, South Korea*

Wonseok Ko − *Department of Energy Science, Sungkyunkwan University (SKKU), Suwon 440-746, South Korea; SKKU Institute of Energy Science and Technology (SIEST), Sungkyunkwan University, Suwon 16419, South Korea*

Jae-Seung Kim − *School of Energy and Chemical Engineering, Ulsan National Institute of Science and Technology (UNIST), Ulsan 44919, South Korea*

Yeji Choi − *Department of Chemical and Biomolecular Engineering, Yonsei University, Seoul 03722, South Korea*

Hyungsub Kim − *Korea Atomic Energy Research Institute, Daejeon 34057, South Korea*

Hiram Kwak − *Department of Chemical and Biomolecular Engineering, Yonsei University, Seoul 03722, South Korea*

Dong-Hwa Seo − *School of Energy and Chemical Engineering, Ulsan National Institute of Science and Technology (UNIST), Ulsan 44919, South Korea*

Jongsoon Kim − *Department of Energy Science, Sungkyunkwan University (SKKU), Suwon 440-746, South Korea; SKKU Institute of Energy Science and Technology (SIEST), Sungkyunkwan University, Suwon 16419, South Korea*

Complete contact information is available at: https://pubs.acs.org/10.1021/acsenergylett.2c01514

Author Contributions

J.P. and J.P.S. contributed equally to this work.

Notes

The authors declare no competing financial interest.

■ ACKNOWLEDGMENTS

This work was supported by the program of phased development of carbon neutral technologies through the National Research Foundation of Korea (NRF) funded by the Ministry of Science, ICT (NRF-2022M3J1A1085397). The computational work was supported by the Supercomputing Center/Korea Institute of Science and Technology Information with supercomputing resources, including technical support (KSC-2021-CRE-0337 to D.-H.S.).

■ REFERENCES

(1) Kim, J.; Lee, J.; You, J.; Park, M.-S.; Al Hossain, M. S.; Yamauchi, Y.; Kim, J. H. Conductive polymers for next-generation energy storage systems: recent progress and new functions. *Mater. Horiz.* **2016**, *3*, 517−535.

(2) Hannan, M.; Hoque, M. M.; Mohamed, A.; Ayob, A. Review of energy storage systems for electric vehicle applications: Issues and challenges. *Renew. Sust. Energy Rev.* **2017**, *69*, 771−789.

(3) Jaskula, B. Lithium Statistics and Information. https://www.usgs.gov/centers/national-minerals-information-center/lithium-statistics-and-information (accessed 2022-06-08).

(4) Kim, S. W.; Seo, D. H.; Ma, X.; Ceder, G.; Kang, K. Electrode materials for rechargeable sodium-ion batteries: potential alternatives to current lithium-ion batteries. *Adv. Energy Mater.* **2012**, *2*, 710−721.

(5) Vikström, H.; Davidsson, S.; Höök, M. Lithium availability and future production outlooks. *Appl. Energy* **2013**, *110*, 252−266.

(6) Hwang, J.-Y.; Myung, S.-T.; Sun, Y.-K. Sodium-ion batteries: present and future. *Chem. Soc. Rev.* **2017**, *46*, 3529−3614.

(7) Abraham, K. How comparable are sodium-ion batteries to lithium-ion counterparts? *ACS Energy Lett.* **2020**, *5*, 3544−3547.

(8) Arbizzani, C.; Gabrielli, G.; Mastragostino, M. Thermal stability and flammability of electrolytes for lithium-ion batteries. *J. Power Sources* **2011**, *196*, 4801−4805.

(9) Wang, J.; Yamada, Y.; Sodeyama, K.; Watanabe, E.; Takada, K.; Tateyama, Y.; Yamada, A. Fire-extinguishing organic electrolytes for safe batteries. *Nat. Energy* **2018**, *3*, 22−29.

(10) Liu, K.; Liu, Y.; Lin, D.; Pei, A.; Cui, Y. Materials for lithium-ion battery safety. *Sci. Rep.* **2018**, *4*, eaas9820.

(11) Shah, J. The Top 5 Lithium-ion Battery Mishaps And Lessons Therein. https://www.saurenergy.com/ev-storage/the-top-5-lithium-ion-battery-mishaps-and-lessons-therein (accessed 2022-06-10).

(12) Park, K. H.; Bai, Q.; Kim, D. H.; Oh, D. Y.; Zhu, Y.; Mo, Y.; Jung, Y. S. Design strategies, practical considerations, and new solution processes of sulfide solid electrolytes for all-solid-state batteries. *Adv. Energy Mater.* **2018**, *8*, 1800035.

(13) Hayashi, A.; Noi, K.; Sakuda, A.; Tatsumisago, M. Superionic glass-ceramic electrolytes for room-temperature rechargeable sodium batteries. *Nat. Commun.* **2012**, *3*, 1−5.

(14) Banerjee, A.; Park, K. H.; Heo, J. W.; Nam, Y. J.; Moon, C. K.; Oh, S. M.; Hong, S. T.; Jung, Y. S. Na_3SbS_4: a solution processable sodium superionic conductor for all-solid-state sodium-ion batteries. *Angew. Chem., Int. Ed.* **2016**, *128*, 9786−9790.

(15) Chu, I.-H.; Kompella, C. S.; Nguyen, H.; Zhu, Z.; Hy, S.; Deng, Z.; Meng, Y. S.; Ong, S. P. Room-temperature all-solid-state rechargeable sodium-ion batteries with a Cl-doped Na_3PS_4 superionic conductor. *Sci. Rep.* **2016**, *6*, 1−10.

(16) Yu, Z.; Shang, S. L.; Seo, J. H.; Wang, D.; Luo, X.; Huang, Q.; Chen, S.; Lu, J.; Li, X.; Liu, Z. K.; et al. Exceptionally High Ionic Conductivity in $Na_3P_{0.62}As_{0.38}S_4$ with Improved Moisture Stability for Solid-State Sodium-Ion Batteries. *Adv. Mater.* **2017**, *29*, 1605561.

(17) Heo, J. W.; Banerjee, A.; Park, K. H.; Jung, Y. S.; Hong, S. T. New Na-ion Solid Electrolytes $Na_{4-x}Sn_{1-x}Sb_xS_4$ ($0.02 \leq x \leq 0.33$) for All-Solid-State Na-ion Batteries. *Adv. Energy Mater.* **2018**, *8*, 1702716.

(18) Duchardt, M.; Ruschewitz, U.; Adams, S.; Dehnen, S.; Roling, B. Vacancy-Controlled Na^+ Superion Conduction in $Na_{11}Sn_2PS_{12}$. *Angew. Chem., Int. Ed.* **2018**, *130*, 1365−1369.

(19) Fuchs, T.; Culver, S. P.; Till, P.; Zeier, W. G. Defect-mediated conductivity enhancements in $Na_{3-x}Pn_{1-x}W_xS_4$ (Pn = P, Sb) using aliovalent substitutions. *ACS Energy Lett.* **2020**, *5*, 146−151.

(20) Asakura, R.; Reber, D.; Duchêne, L.; Payandeh, S.; Remhof, A.; Hagemann, H.; Battaglia, C. 4 V room-temperature all-solid-state sodium battery enabled by a passivating cathode/hydroborate solid electrolyte interface. *Energy Environ. Sci.* **2020**, *13*, 5048−5058.

(21) Duchêne, L.; Kim, D. H.; Song, Y. B.; Jun, S.; Moury, R.; Remhof, A.; Hagemann, H.; Jung, Y. S.; Battaglia, C. Crystallization of closo-borate electrolytes from solution enabling infiltration into slurry-casted porous electrodes for all-solid-state batteries. *Energy Storage Mater.* **2020**, *26*, 543−549.

(22) Heinz, M. V.; Graeber, G.; Landmann, D.; Battaglia, C. Pressure management and cell design in solid-electrolyte batteries, at the example of a sodium-nickel chloride battery. *J. Power Sources* **2020**, *465*, 228268.

(23) Schlem, R.; Banik, A.; Eckardt, M.; Zobel, M.; Zeier, W. G. $Na_{3-x}Er_{1-x}Zr_xCl_6$—A Halide-Based Fast Sodium-ion Conductor with Vacancy-Driven Ionic Transport. *ACS Appl. Energy Materials* **2020**, *3*, 10164−10173.

(24) Tsuji, F.; Nasu, A.; Sakuda, A.; Tatsumisago, M.; Hayashi, A. Mechanochemical synthesis and characterization of $Na_{3-x}P_{1-x}W_xS_4$ solid electrolytes. *J. Power Sources* **2021**, *506*, 230100.

(25) Kwak, H.; Lyoo, J.; Park, J.; Han, Y.; Asakura, R.; Remhof, A.; Battaglia, C.; Kim, H.; Hong, S.-T.; Jung, Y. S. Na_2ZrCl_6 enabling highly stable 3 V all-solid-state Na-ion batteries. *Energy Storage Mater.* **2021**, *37*, 47−54.

(26) Chi, X.; Zhang, Y.; Hao, F.; Kmiec, S.; Dong, H.; Xu, R.; Zhao, K.; Ai, Q.; Terlier, T.; Wang, L.; et al. An electrochemically stable homogeneous glassy electrolyte formed at room temperature for all-solid-state sodium batteries. *Nat. Commun.* **2022**, *13*, 1−11.

(27) Jung, Y. S.; Oh, D. Y.; Nam, Y. J.; Park, K. H. Issues and challenges for bulk-type all-solid-state rechargeable lithium batteries using sulfide solid electrolytes. *Isr. J. Chem.* **2015**, *55*, 472−485.

(28) Richards, W. D.; Miara, L. J.; Wang, Y.; Kim, J. C.; Ceder, G. Interface stability in solid-state batteries. *Chem. Mater.* **2016**, *28*, 266−273.

(29) Yu, C.; Ganapathy, S.; De Klerk, N. J.; van Eck, E. R.; Wagemaker, M. Na-ion dynamics in tetragonal and cubic Na_3PS_4, a Na-ion conductor for solid state Na-ion batteries. *J. Mater. Chem. A* **2016**, *4*, 15095−15105.

(30) Moon, C. K.; Lee, H.-J.; Park, K. H.; Kwak, H.; Heo, J. W.; Choi, K.; Yang, H.; Kim, M.-S.; Hong, S.-T.; Lee, J. H.; et al. Vacancy-driven Na^+ superionic conduction in new Ca-doped Na_3PS_4 for all-solid-state Na-ion batteries. *ACS Energy Lett.* **2018**, *3*, 2504−2512.

(31) Han, Y.; Jung, S. H.; Kwak, H.; Jun, S.; Kwak, H. H.; Lee, J. H.; Hong, S. T.; Jung, Y. S. Single-or Poly-Crystalline Ni-Rich Layered Cathode, Sulfide or Halide Solid Electrolyte: Which Will be the Winners for All-Solid-State Batteries? *Adv. Energy Mater.* **2021**, *11*, 2100126.

(32) Weng, W.; Liu, G.; Li, Y.; Shen, L.; Yao, X. Tungsten and oxygen co-doped stable tetragonal phase Na_3SbS_4 with ultrahigh ionic conductivity for all-solid-state sodium batteries. *Appl. Mater. Today* **2022**, *27*, 101448.

(33) Zhang, Z.; Ramos, E.; Lalère, F.; Assoud, A.; Kaup, K.; Hartman, P.; Nazar, L. F. $Na_{11}Sn_2PS_{12}$: a new solid state sodium superionic conductor. *Energy Environ. Sci.* **2018**, *11*, 87−93.

(34) Kwak, H.; Wang, S.; Park, J.; Liu, Y.; Kim, K. T.; Choi, Y.; Mo, Y.; Jung, Y. S. Emerging Halide Superionic Conductors for All-Solid-State Batteries: Design, Synthesis, and Practical Applications. *ACS Energy Lett.* **2022**, *7*, 1776−1805.

(35) Asano, T.; Sakai, A.; Ouchi, S.; Sakaida, M.; Miyazaki, A.; Hasegawa, S. Solid halide electrolytes with high lithium-ion conductivity for application in 4 V class bulk-type all-solid-state batteries. *Adv. Mater.* **2018**, *30*, 1803075.

(36) Li, X.; Liang, J.; Luo, J.; Banis, M. N.; Wang, C.; Li, W.; Deng, S.; Yu, C.; Zhao, F.; Hu, Y. Air-stable Li_3InCl_6 electrolyte with high voltage compatibility for all-solid-state batteries. *Energy Environ. Sci.* **2019**, *12*, 2665−2671.

(37) Liang, J.; Li, X.; Wang, S.; Adair, K. R.; Li, W.; Zhao, Y.; Wang, C.; Hu, Y.; Zhang, L.; Zhao, S.; et al. Site-occupation-tuned superionic Li_xScCl_{3+x} halide solid electrolytes for all-solid-state batteries. *J. Am. Chem. Soc.* **2020**, *142*, 7012−7022.

(38) Zhou, L.; Kwok, C. Y.; Shyamsunder, A.; Zhang, Q.; Wu, X.; Nazar, L. F. A new halospinel superionic conductor for high-voltage all solid state lithium batteries. *Energy Environ. Sci.* **2020**, *13*, 2056–2063.

(39) Kwak, H.; Han, D.; Lyoo, J.; Park, J.; Jung, S. H.; Han, Y.; Kwon, G.; Kim, H.; Hong, S. T.; Nam, K. W.; et al. New Cost-Effective Halide Solid Electrolytes for All-Solid-State Batteries: Mechanochemically Prepared Fe^{3+}-Substituted Li_2ZrCl_6. *Adv. Energy Mater.* **2021**, *11*, 2003190.

(40) Kwak, H.; Han, D.; Son, J. P.; Kim, J. S.; Park, J.; Nam, K.-W.; Kim, H.; Jung, Y. S. Li^+ conduction in aliovalent-substituted monoclinic Li_2ZrCl_6 for all-solid-state batteries: $Li_{2+x}Zr_{1-x}M_xCl_6$ (M= In, Sc). *Chem. Eng. J.* **2022**, *437*, 135413.

(41) Park, K.-H.; Kaup, K.; Assoud, A.; Zhang, Q.; Wu, X.; Nazar, L. F. High-voltage superionic halide solid electrolytes for all-solid-state Li-ion batteries. *ACS Energy Lett.* **2020**, *5*, 533–539.

(42) Park, J.; Han, D.; Kwak, H.; Han, Y.; Choi, Y. J.; Nam, K.-W.; Jung, Y. S. Heat treatment protocol for modulating ionic conductivity via structural evolution of $Li_{3-x}Yb_{1-x}M_xCl_6$ (M= Hf^{4+}, Zr^{4+}) new halide superionic conductors for all-solid-state batteries. *Chem. Eng. J.* **2021**, *425*, 130630.

(43) Kim, S. Y.; Kaup, K.; Park, K.-H.; Assoud, A.; Zhou, L.; Liu, J.; Wu, X.; Nazar, L. F. Lithium ytterbium-based halide solid electrolytes for high voltage all-solid-state batteries. *ACS Mater. Lett.* **2021**, *3*, 930–938.

(44) Schlem, R.; Muy, S.; Prinz, N.; Banik, A.; Shao-Horn, Y.; Zobel, M.; Zeier, W. G. Mechanochemical synthesis: a tool to tune cation site disorder and ionic transport properties of Li_3MCl_6 (M= Y, Er) superionic conductors. *Adv. Energy Mater.* **2020**, *10*, 1903719.

(45) Shi, X.; Zeng, Z.; Sun, M.; Huang, B.; Zhang, H.; Luo, W.; Huang, Y.; Du, Y.; Yan, C. Fast Li-ion Conductor of Li_3HoBr_6 for Stable All-Solid-State Lithium–Sulfur Battery. *Nano Lett.* **2021**, *21*, 9325–9331.

(46) Plass, M. A.; Bette, S.; Dinnebier, R. E.; Lotsch, B. V. Enhancement of Superionic Conductivity by Halide Substitution in Strongly Stacking Faulted $Li_3HoBr_{6-x}I_x$ Phases. *Chem. Mater.* **2022**, *34*, 3227–3235.

(47) Wu, E.; Banerjee, S.; Tang, H.; Richardson, P. M.; Doux, J.-M.; Qi, J.; Zhu, Z.; Grenier, A.; Li, Y.; Zhao, E. A Stable Cathode-Solid Electrolyte Composite for Long-Cycle-Life, High Voltage Solid-State Sodium-ion Batteries. *Nat. Commun.* **2021**, *12*, 1256.

(48) Yi, L.; Ji, Y.; Shao, P.; Chen, J.; Li, J.; Li, H.; Chen, K.; Peng, X.; Wen, Z. Scalable Synthesis of Tungsten Disulfide Nanosheets for Alkali-Acid Electrocatalytic Sulfion Recycling and H_2 Generation. *Angew. Chem. Inter. Ed.* **2021**, *60*, 21550–21557.

(49) Yao, T.; Yang, H.; Wang, K.; Jiang, H.; Chen, X.-B.; Liu, H.; Wang, Q.; Ding, W. Effects of additive NaI on electrodeposition of Al coatings in $AlCl_3$-NaCl-KCl molten salts. *Front. Chem. Sci. Eng.* **2021**, *15*, 138–147.

(50) Lee, Y.; Kim, H.-J.; Byun, D.-J.; Cho, K.-K.; Ahn, J.-H.; Kim, C.-S. Electrochemically activated Na–$ZnCl_2$ battery using a carbon matrix in the cathode compartment. *J. Power Sources* **2019**, *440*, 227110.

(51) Ellis, B. L.; Nazar, L. F. Sodium and sodium-ion energy storage batteries. *Curr. Opin. Solid State Mater. Sci.* **2012**, *16*, 168–177.

(52) Qingfeng, L.; Hjuler, H. A.; Berg, R. W.; Bjerrum, N. Influence of substrates on the electrochemical deposition and dissolution of aluminum in $NaAlCl_4$ melts. *J. Electrochem. Soc.* **1991**, *138*, 763.

(53) Kravchyk, K. V.; Wang, S.; Piveteau, L.; Kovalenko, M. V. Efficient aluminum chloride–natural graphite battery. *Chem. Mater.* **2017**, *29*, 4484–4492.

(54) Xue, L.; Xin, S.; Goodenough, J. B.; Angell, C. A. An inverse aluminum battery: Putting the aluminum as the cathode. *ACS Energy Lett.* **2017**, *2*, 1534–1538.

(55) Zhan, X.; Bonnett, J. F.; Engelhard, M. H.; Reed, D. M.; Sprenkle, V. L.; Li, G. A High-Performance Na–Al Battery Based on Reversible $NaAlCl_4$ Catholyte. *Adv. Energy Mater.* **2020**, *10*, 2001378.

(56) Kühnl, H.; Strumpf, A.; Gladziwa, M. Die systeme des typs $MCl/AlCl_3/SO_2$ (M= Li, Na, K, NH_4). *Z. Anorg. Allg. Chem.* **1979**, *449*, 145–156.

(57) Song, J.; Jeong, G.; Lee, A.-J.; Park, J. H.; Kim, H.; Kim, Y.-J. Dendrite-free polygonal sodium deposition with excellent interfacial stability in a $NaAlCl_4$–$2SO_2$ inorganic electrolyte. *ACS Appl. Mater. Interfaces* **2015**, *7*, 27206–27214.

(58) Chen, J.; Fan, X.; Li, Q.; Yang, H.; Khoshi, M. R.; Xu, Y.; Hwang, S.; Chen, L.; Ji, X.; Yang, C.; et al. Electrolyte design for LiF-rich solid–electrolyte interfaces to enable high-performance micro-sized alloy anodes for batteries. *Nat. Energy* **2020**, *5*, 386–397.

(59) Zhou, L.; Zuo, T.-T.; Kwok, C. Y.; Kim, S. Y.; Assoud, A.; Zhang, Q.; Janek, J.; Nazar, L. F. High areal capacity, long cycle life 4 V ceramic all-solid-state Li-ion batteries enabled by chloride solid electrolytes. *Nat. Energy* **2022**, 1–11.

(60) Weppner, W.; Huggins, R. Ionic conductivity of alkali metal chloroaluminates. *Phys. Lett. A* **1976**, *58*, 245–248.

(61) Tanibata, N.; Takimoto, S.; Nakano, K.; Takeda, H.; Nakayama, M.; Sumi, H. Metastable Chloride Solid Electrolyte with High Formability for Rechargeable All-Solid-State Lithium Metal Batteries. *ACS Mater. Lett.* **2020**, *2*, 880–886.

(62) Liu, Y.; Wang, S.; Nolan, A. M.; Ling, C.; Mo, Y. Tailoring the Cation Lattice for Chloride Lithium-Ion Conductors. *Adv. Energy Mater.* **2020**, *10*, 2002356.

(63) Ito, H.; Shitara, K.; Wang, Y.; Fujii, K.; Yashima, M.; Goto, Y.; Moriyoshi, C.; Rosero-Navarro, N. C.; Miura, A.; Tadanaga, K. Kinetically Stabilized Cation Arrangement in Li_3YCl_6 Superionic Conductor during Solid-State Reaction. *Adv. Sci.* **2021**, *8*, 2101413.

(64) Mairesse, G.; Barbier, P.; Wignacourt, J.-P. Comparison of the crystal structures of alkaline (M= Li, Na, K, Rb, Cs) and pseudo-alkaline (M= NO, NH_4) tetrachloroaluminates, $MAlCl_4$. *Acta Crystallographica Section B: Structural Crystallography and Crystal Chemistry* **1979**, *35*, 1573–1580.

(65) Kim, K.; Park, D.; Jung, H.-G.; Chung, K. Y.; Shim, J. H.; Wood, B. C.; Yu, S. Material design strategy for halide solid electrolytes Li_3MX_6 (X= Cl, Br, and I) for all-solid-state high-voltage Li-ion batteries. *Chem. Mater.* **2021**, *33*, 3669–3677.

(66) Shannon, R. T.; Prewitt, C. T. Effective ionic radii in oxides and fluorides. *Acta Crystallographica Section B: Structural Crystallography and Crystal Chemistry* **1969**, *25*, 925–946.

(67) Doorenbos, H. E.; Evans, J. C.; Kagel, R. Preparation, Raman, and nuclear quadrupole resonance data for the complex SCl_3^+ $AlCl_4^-$. *J. Phys. Chem.* **1970**, *74*, 3385–3387.

(68) Ahmed, E.; Koehler, D.; Ruck, M. Room-Temperature Synthesis of Bismuth Clusters in Ionic Liquids and Crystal Growth of $Bi_5(AlCl_4)_3$. *Z. Anorg. Allg. Chem.* **2009**, *635*, 297–300.

(69) Krebs, B.; Greiwing, H.; Brendel, C.; Taulelle, F.; Gaune-Escard, M.; Berg, R. W. Crystallographic and aluminum-27 NMR study on premelting phenomena in crystals of sodium tetrachloroaluminate. *Inorg. Chem.* **1991**, *30*, 981–988.

(70) Chen, H.; Wong, L. L.; Adams, S. SoftBV–a software tool for screening the materials genome of inorganic fast ion conductors. *Acta Crystallographica Section B: Structural Science, Crystal Engineering and Materials* **2019**, *75*, 18–33.

(71) Zhang, W.; Oganov, A. R.; Goncharov, A. F.; Zhu, Q.; Boulfelfel, S. E.; Lyakhov, A. O.; Stavrou, E.; Somayazulu, M.; Prakapenka, V. B.; Konôpková, Z. Unexpected stable stoichiometries of sodium chlorides. *Science* **2013**, *342*, 1502–1505.

(72) Zhang, Z.; Meng, Y.; Wang, Y.; Yuan, H.; Xiao, D. Obtaining P2-$Na_{0.56}[Ni_{0.1}Co_{0.1}Mn_{0.8}]O_2$ Cathode Materials for Sodium-ion Batteries by using a Co-precipitation Method. *ChemElectroChem.* **2018**, *5*, 3229–3235.

(73) Ren, Z.; Wang, M.; Chen, S.; Ding, L.; Li, H.; Liu, J.; Zheng, J.; Liu, Z.; Wang, D.; Wang, M. Improvement of Cyclic Stability of $Na_{0.67}Mn_{0.8}Ni_{0.1}Co_{0.1}O_2$ via Suppressing Lattice Variation. *Chin. Phys. Lett.* **2021**, *38*, 076102.

(74) Zhang, W.; Leichtweiß, T.; Culver, S. P.; Koerver, R.; Das, D.; Weber, D. A.; Zeier, W. G.; Janek, J. The detrimental effects of carbon

https://doi.org/10.1021/acsenergylett.2c01514
ACS Energy Lett. 2022, 7, 3293–3301

additives in $Li_{10}GeP_2S_{12}$-based solid-state batteries. *ACS Appl. Mater. Interfaces* **2017**, *9*, 35888−35896.
(75) Lacivita, V.; Wang, Y.; Bo, S.-H.; Ceder, G. Ab initio investigation of the stability of electrolyte/electrode interfaces in all-solid-state Na batteries. *J. Mater. Chem. A* **2019**, *7*, 8144−8155.

https://doi.org/10.1021/acsenergylett.2c01514
ACS Energy Lett. 2022, 7, 3293−3301